Experiments in Fluids (2006) 40: 847–858
DOI 10.1007/s00348-006-0123-z

RESEARCH ARTICLE

Evelyn N. Wang · Shankar Devasenathipathy
Hao Lin · Carlos H. Hidrovo · Juan G. Santiago
Kenneth E. Goodson · Thomas W. Kenny

A hybrid method for bubble geometry reconstruction in two-phase microchannels

Received: 7 July 2005 / Revised: 11 January 2006 / Accepted: 15 January 2006 / Published online: 30 March 2006

Abstract Understanding bubble dynamics is critical to the design and optimization of two-phase microchannel heat sinks. This paper presents a hybrid experimental and computational methodology that reconstructs the three-dimensional bubble geometry, as well as provides other critical information associated with nucleating bubbles in microchannels. Rectangular cross-section silicon microchannels with hydraulic diameters less than 200 μm were fabricated with integrated heaters for the flow experiments, and the working liquid used was water. Bubbles formed via heterogeneous nucleation and were observed to grow from the silicon side walls of the channels. Two-dimensional images and two-component liquid velocity field measurements during bubble growth were obtained using micron-resolution particle image velocimetry (μPIV). These measurements were combined with iterative three-dimensional numerical simulations using finite element software, FEMLAB. The three-dimensional shape and location of the bubble were quantified by identifying the geometry that provided the best match between the computed flow field and the μPIV data. The reconstructed flow field through this process reproduced the experimental data within an error of 10–20%. Other important information such as contact angles and bubble growth rates can also be estimated from this methodology. This work is an important step toward understanding the physical mechanisms behind bubble growth and departure.

E. N. Wang (✉) · S. Devasenathipathy · H. Lin
C. H. Hidrovo · J. G. Santiago · K. E. Goodson · T. W. Kenny
Department of Mechanical Engineering, Stanford University,
Stanford, CA 94305-3030, USA
E-mail: enwang@stanford.edu
Tel.: +1-650-7360044
Fax: +1-650-7233521

Present address: S. Devasenathipathy
Department of Molecular Pharmacology, Stanford University,
Stanford, CA 94305, USA

Present address: E. N. Wang
Bell Laboratories, Lucent Technologies,
Murray Hill, NJ 07974, USA

Present address: H. Lin
Department of Mechanical and Aerospace Engineering,
Rutgers University, Piscataway, NJ 08854, USA

1 Introduction

Interest in cooling microprocessors using microchannel heat sinks has significantly increased in the past decade, due to advancements in micromachining technology and increases in chip power density (International Technology Roadmap for Semiconductors, http://www.public.itrs.net). Two-phase microchannel heat sinks provide a potential solution where large heat generation is present, because latent heat during the phase-change process can be leveraged to capture and transfer high heat fluxes. Implementation of two-phase microchannels, however, is challenging due to the instability of the vapor bubbles and slugs, leading to local dry-out and subsequently poor cooling in such regions (Kennedy et al. 2000; Hetsroni et al. 2001). Efforts have therefore focused on the understanding of flow patterns during microchannel boiling, which are different than their macroscale counterparts (Jiang et al. 2001; Zhang et al. 2002, 2005; Peng and Wang 1993; Hetsroni et al. 2002; Kandlikar 2004; Mukherjee and Kandlikar 2005). Insights provided by such studies are essential for the development and optimization of two-phase microchannel cooling solutions.

As a step toward understanding microchannel boiling behavior, incipient boiling has been examined in which bubbles nucleate, grow, and depart from nucleation sites on channel walls. Many studies have used flow visualization with high-speed cameras and white light microscopy to aid in understanding mechanisms and the associated forces exerted during bubble nucleation and departure (Kandlikar and Stumm 1995; Lee et al. 2004; Qu and Mudawar 2002). Lee et al. (2004) reported

bubble growth rates, departure sizes, and departure frequencies for a single trapezoidal microchannel geometry with $D_h = 41.3$ μm (where D_h denotes hydraulic diameter) using a high-speed camera and commercial edge detection software. They reported that bubble diameter was often linear with time and bubble departure radii were in good agreement with a modified Levy model (Levy 1967). Their work provides important data regarding bubble dynamics during incipient boiling as well as comparisons with classical models.

Recent modeling developments have contributed to understanding growth of vapor bubbles in microchannels. Mukherjee and Kandlikar (2005) used the level set technique to numerically model the growth dynamics. In addition, various modeling efforts have also been combined with white light imaging techniques to enable better predictions relevant to microscale incipient boiling processes. Qu and Mudawar (2002) developed a model predicting incipient heat flux based on visualization experiments performed in microchannels of $D_h = 350$ μm. Kandlikar and Stumm (1995) on the other hand, measured bubble departure radii and contact angles in channels with $D_h = 5.7$ mm to supplement a control volume based bubble departure model. In the last two cases, model predictions relied on assumptions of bubble shape, location, liquid velocity fields, and associated surface forces since experimental data on these quantities were limited.

Liquid velocity fields in general two-phase systems can be obtained using particle image velocimetry (PIV) (Qiu and Dhir 2002; Lindken and Merzkirch 2002; Liu et al. 2004; Park et al. 2004). Qiu and Dhir (2002) used PIV to examine the local flow fields surrounding sliding bubbles on heated inclined surfaces: vortical structures were observed in the rear region of the bubble which confirmed their temperature fringe pattern results. Lindken and Merzkirch (2000, 2002) developed a technique using PIV and shadowgraphy to measure velocity fields in bubbly two-phase flow. They used this measurement technique to investigate turbulent structures induced by gas bubbles. Park et al. (2002, 2004) suggested the possibility of using confocal microscopy with micron-resolution PIV (μPIV) to capture velocity fields surrounding slowly moving air slugs at several depths to reconstruct the three-dimensional liquid film and velocity field. However, the latter technique would be very limited by the low temporal resolution of confocal imaging for both image capture and variations of the location of the focal plane. Despite these limitations, these studies suggest that velocity field measurements can potentially provide valuable data and insight that can complement white light imaging and shed more insight into bubble dynamics and departure.

In this work, we present a hybrid experimental and computational methodology to reconstruct the three-dimensional bubble geometry in microchannels with the use of μPIV and numerical simulations. This work contributes toward the understanding of dynamics and mechanisms for bubble growth and departure by providing quantitative information on bubble diameter, location, contact angles, growth rate, and bubble motion. This information can be integrated to provide estimates of the three-dimensional flow field which can be used for force analyses.

We first used μPIV measurements in microchannels with $D_h = 190$ μm to obtain two-dimensional liquid-phase velocity fields surrounding nucleating bubbles. To avoid difficulties associated with real-time control of the location of the measurement volume, we chose to obtain velocity fields at a single channel depth during one nucleation-to-departure cycle (see the exemplary result in Fig. 2). These transient measurements provide two-component velocity fields in two-dimensional planes of the three-dimensional flow field. Nonetheless, by combining this information with iterative numerical simulations (FEMLAB, http://www.comsol.com), it is possible to approximately reconstruct the three-dimensional bubble geometry as well as the flow field. This hybrid experimental and computational methodology is the primary focus of the current paper.

This paper is organized as follows: The experimental setup is summarized in Sect. 2, together with typical μPIV measurement results. In Sects. 3 and 4, we present the hybrid experimental and numerical methodology and results, respectively. In Sect. 5, we draw conclusions and make suggestions for future work. Estimates of uncertainties associated with the measurement and methodology are presented in Appendix.

2 Experimental setup

2.1 Device fabrication and flow delivery

A schematic of the experimental setup and microchannel test device is shown in Fig. 1. The device was fabricated using standard micromachining techniques. The microchannel was deep reactive ion etched (DRIE) on a silicon substrate and was 2 cm long, 200 μm wide, and 180 μm deep ($D_h = 190$ μm). These dimensions correspond to the coordinate directions x, y, and z, respectively. The DRIE process created fine features on the side walls with approximate roughness ranging from 0.1 to 0.4 μm and occasionally larger defects ranging from 2 to 5 μm, which probably acted as nucleation sites for bubbles (Zhang et al. 2005). A localized titanium heater of 1 mm^2 area was patterned in the middle of the channel back side. Titanium thin-film temperature sensors were fabricated 1 mm upstream and 1 mm downstream of the heater to measure approximately 1 mm^2 area-averaged wall temperatures. A glass slide (Pyrex) was anodically bonded to the silicon channel which allowed for flow visualization during the bubble growth process. Wire bonds electrically connected the heater and temperature sensors to the printed circuit board, where an input heater voltage could be applied and

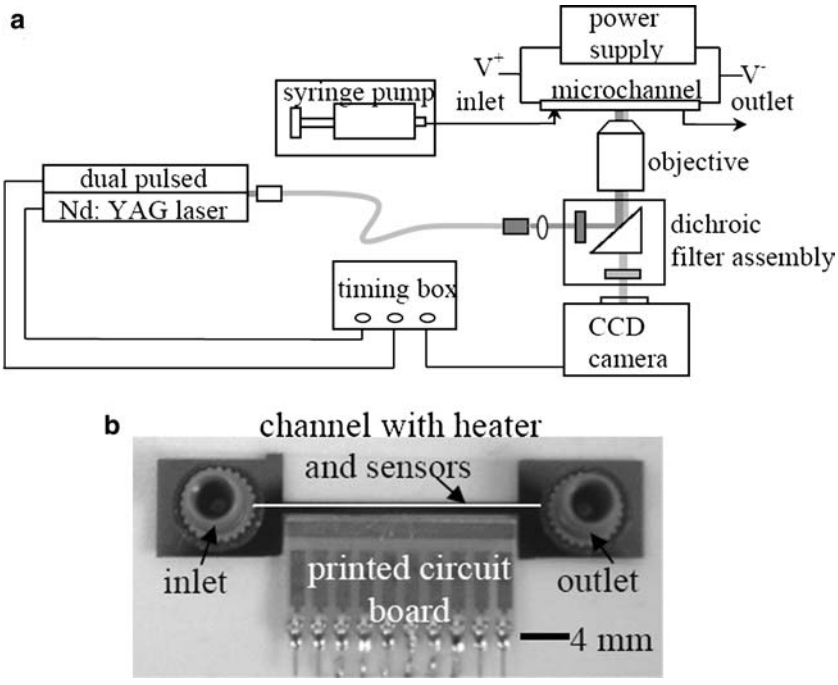

Fig. 1 Schematic of experimental setup with fabricated microchannel device with integrated, thin-film heaters and temperature sensors: **a** schematic and **b** image of microfabricated silicon channel test device viewed from the backside. A *white horizontal line* superimposed on the image indicates the location of the channel on the front side

sensor voltages measured to determine wall temperature. Fluidic inlet and outlet ports (Upchurch Scientific) were glued to the backside of the chip.

The flow was delivered by a constant flow rate syringe pump (PhD 2000, Harvard Apparatus). The working fluid (deionized water) was seeded with 1 μm fluorescent polystyrene particles to a volume density of 0.05%. The particles (Molecular Probes) had a peak excitation wavelength of 540 nm and a peak emission wavelength of 560 nm. Triton X-100 surfactant (Sigma Corporation) was added at a concentration of 0.005% by volume to the particle solution to decrease the effects of particle flocculation and adsorption to channel walls (the critical micelle concentration for this surfactant is 0.01% by volume). We applied typical flow rates of 0.1 ml/min ($Re_D = 10$, where Re_D is Reynolds number based on hydraulic diameter). These flow rates are within the range used in microchannel cooling research (Zhang et al. 2002).

2.2 Flow visualization and μPIV measurements

An epi-fluorescent microscope (Nikon TE300) was integrated with a dual-pulsed Nd:YAG laser (New Wave, Minilase System) as an illumination source (Devasenathipathy et al. 2003). The 532 nm frequency doubled emission of the laser was routed through an optical fiber (Oriel Instruments) to the sample for illumination of the entire device test section volume. A filter cube assembly containing a 532 nm exciter filter, a dichroic beam splitter with a cut-on wavelength of 545 nm, and a 555 nm long-pass barrier emission filter was used to filter and separate the excitation light from the emission signal. The images were captured with a 20× objective (NA = 0.45) and a 12-bit interline transfer cooled CCD camera (Roper Scientific CoolSnap HQ). We used air immersion lenses in effort to be thermally decoupled from the experiment. The camera had a 1,300×1,040 pixel array with square pixels 6.45 μm on a side. We used 2×2 on-chip pixel binning during image acquisition. The bubble diameters grew at a typical rate of 5 μm/s for an applied power of 0.58 W. The corresponding wall temperature for these nucleating bubbles was measured to be approximately 60°C. (Local absolute pressure at the bubble site is estimated to be 1.0 atm.) Previous studies have shown a decrease in incipient boiling temperature by increasing the air content in water (Murphy and Bergles 1972; Steinke and Kandlikar 2004). However, the low measured temperatures of our study strongly indicate that the bubble nucleation and growth we observed might be mostly attributed to the outgassing of dissolved gases (e.g., carbon dioxide, nitrogen, and oxygen, etc.), not boiling. We also hypothesize that residual gases trapped in cavities on the silicon channel walls provided nucleation sites for such outgassing. As discussed by Jones et al. (1999), such nucleation sites reduce the energy barrier for nucleation to occur at relatively low temperatures. Similar behavior has been observed at comparable temperatures and pressures (Jiang et al. 2001; Li and Cheng 2004; Klein et al. 2005). The distinction and interaction between outgassing and incipient boiling in microchannels is an important area that warrants further investigation, and may lead to different growth rates and departure characteristics. Local wall temperature and pressure measurements are critical to such study.

Liquid velocity fields around growing bubbles were measured using μPIV (Santiago et al. 1998). A custom PIV algorithm was used to interrogate the images and determine time-averaged velocity fields using the average cross-correlation method (Meinhart et al. 2005). Typical time between frames was 200 μs for 0.1 ml/min flow rates. Three pairs of images were used in the correlation algorithm and each pair of images was separated by 222 ms. We assumed that the bubbles were approximately quasi-stationary during acquisition of these three image pairs. The measurement depth defined as twice the distance from the focal plane where particle-image intensity is sufficiently low such that it will not significantly influence the velocity measurement is 13.5 μm based on diffraction limits, geometrical optics, and the finite size of the particle (Meinhart et al. 2000).

2.3 Velocity field measurement

An example experimental image for the μPIV measurement is shown in Fig. 2a. The imaged channel section was 450 μm long (in the x, streamwise direction) and 200 μm wide (in the y, spanwise direction). This image was taken at a depth of $d_2 = 17.5$ μm, where d_2 denotes the distance of the focal plane from the inner side of the glass channel wall (see Fig. 3b). The imaging depth into the channel was determined by first focusing on particles adsorbed to the inner glass wall of the channel and then moving the focal plane using the microscopes stage. The total channel depth (into the page) was 180 μm. The corresponding measured velocity field is shown in Fig. 2b; note that this velocity field is a two-component velocity measurement of the full three-dimensional velocity field at a particular focal plane. The measurements can be interpreted as projections of the three-dimensional velocity field onto the focal plane. Similarly, the cross-section of the three-dimensional bubble at this channel depth was a truncated disk with a radius of $a_0 = 48.5$ μm. Uncertainties associated with the flow field measurements and the methodology were approximately 10%. Details of these errors and associated uncertainties are given in Appendix.

Velocity data were obtained at various times (including various stages of bubble growth) for single bubble nucleation-to-departure cycles. We also varied the location of the focal plane to obtain velocity fields for bubbles originating from the same nucleation site at different depths of the channel, specifically, at $d_2 = 10$, 17.5, and 30 μm. In some cases, the bubble nucleation and departure cycle was reproducible enough to warrant a comparison across imaging plane locations (i.e., across realizations of the bubble nucleation and departure cycle).

3 Bubble geometry and flow field reconstruction method

The bubble image and μPIV measurements discussed above provide limited information. They yield a two-component velocity measurement in a two-dimensional

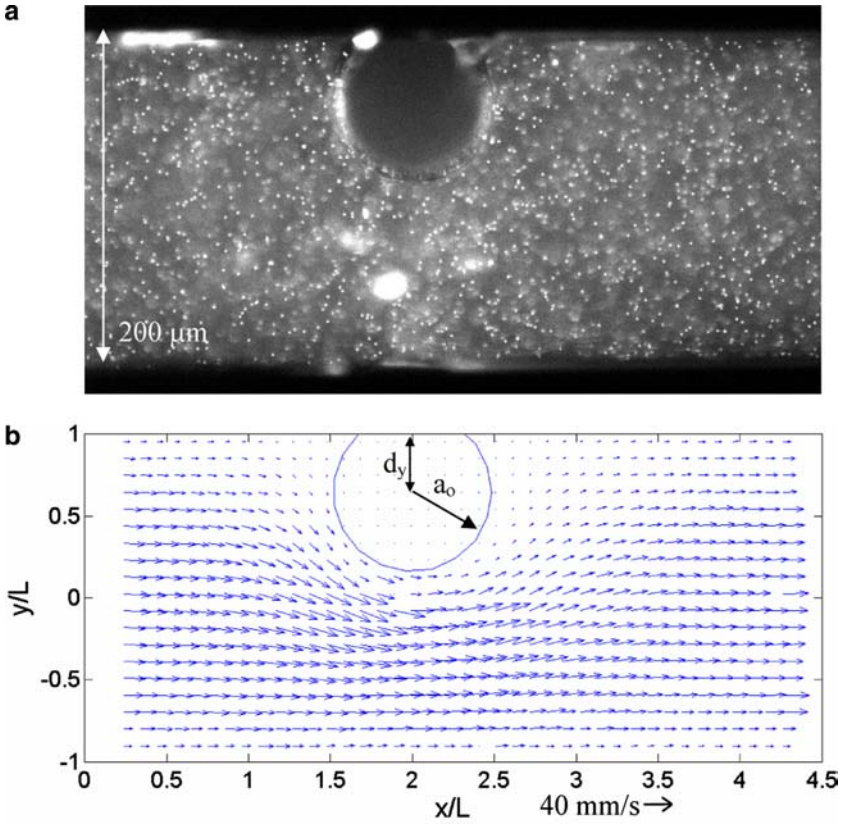

Fig. 2 Example image (**a**) and measured μPIV velocity field surrounding the bubble (**b**). The focal plane was a distance of $d_2 = 17.5$ μm from the glass channel wall (see Fig. 3). The image shows a 450 μm section (in the streamwise, x direction) of a 200 μm wide (in the spanwise, y direction) channel, and the channel depth (into the page) is 180 μm. The bubble image is a truncated disk of $a_0 = 48.5$ μm which represents the cross-section of its full three-dimensional geometry at the focal plane. The coordinates in graph (**b**) are scaled with the half-channel width of $L = 100$ μm. Note that the measurement shows the two-component velocity field of the three-dimensional flow field in the microchannel

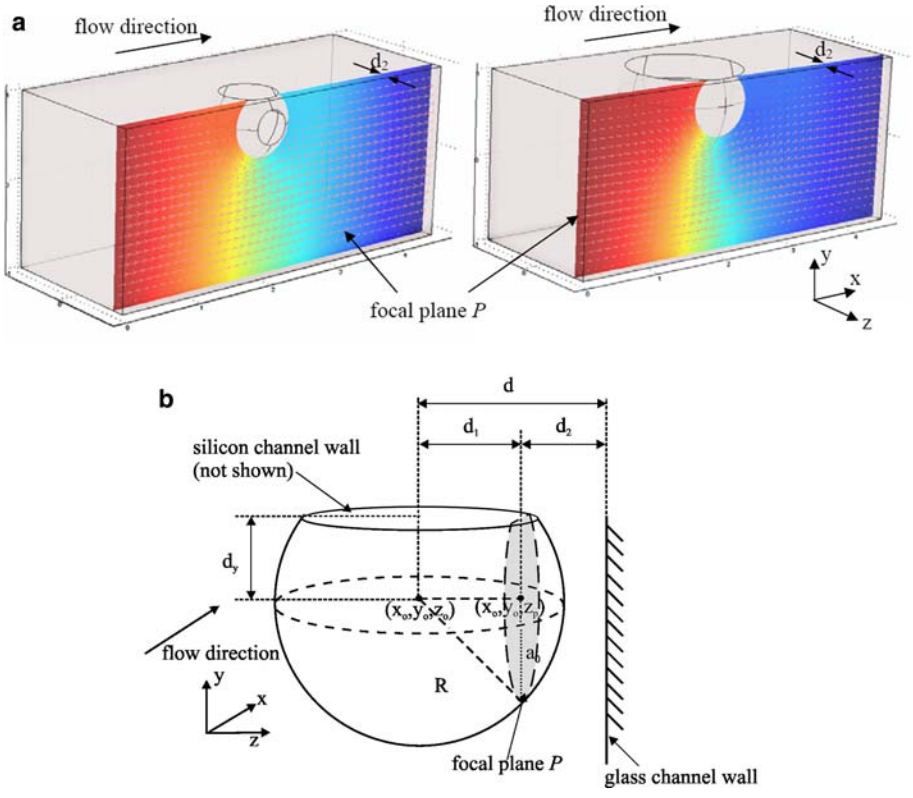

Fig. 3 Schematic for bubble geometry reconstruction. Shown in **a** are two possible bubble geometries in the microchannel where they have identical cross-sectional areas at focal plane P matching the truncated disk shown in Fig. 2. These geometries produce distinctly different flow fields which are compared with the μPIV data to determine the best match. Part **b** shows a schematic of the trial bubble geometry. The bubble may contact both the glass (in the positive z direction) and silicon (in the positive y direction) channel walls when $R > d$ and/or $R > d_y$, respectively. The bubble radius R and center-to-image-plane distance d_1 need to satisfy Eq. 1, leaving R to be the single degree of freedom

slice of the three-dimensional flow. In this section we present a hybrid experimental and numerical method to reconstruct the full three-dimensional flow field as well as bubble geometry.

Our basic approach is as follows. Shown in Fig. 3a are two possibilities of the instantaneous three-dimensional bubble geometry, both with the same cross-sectional area matching the truncated disk with radius a_0 (as shown in Fig. 2a, b) at the focal plane P at a distance d_2 from the inner glass channel wall. Although these two example cases have identical bubble cross-sections, the three-dimensional flow fields surrounding the bubbles have distinctly different two-component velocity fields at the two-dimensional slice of interest. We can therefore predict a variety of three-dimensional flow solutions for bubbles with varying diameters (and varying center locations) but identical bubble cross-sections. The in-plane projection of the predicted three-dimensional velocity vectors at the focal plane can be compared to the respective μPIV measurements and the best match between the predicted and measured velocity fields gives an estimate of the actual bubble geometry.

3.1 Assumptions

We shall employ three important assumptions for our bubble geometry and flow field reconstruction methodology:

1. The bubbles are assumed to be truncated spheres. Typical Reynolds numbers based on bubble diameter are on the order of $Re \sim 10$. The Weber number, which signifies the relative importance of inertial forces to surface tension, is typically on the order of $We \sim 0.01$. This scaling suggests that the bubble undergoes minimal shape deformation and remains nearly spherical. However, at later stages of bubble growth, when bubbles often occupy a large portion of the channel, deformation may be significant due to substantial surface force variations, non-uniform pressure fields in the flow, and contact angle hysteresis. In these situations, the sphericity assumption may not be valid and a more complex geometry may be needed.
2. Bubble location and diameter are assumed to be approximately fixed during the 444 ms duration of our three image pair acquisition. For the current experiments, bubble diameters typically grow at a rate of 5 μm/s; a change of approximately 2 μm during image acquisition. The flow field is also assumed to be quasi-steady. The Strouhal number, based on the growth rate of the bubble (5 μm/s) and the characteristic velocity (40 mm/s) is on the order of $St \sim 10^{-4}$, suggesting unsteady flow effects are insignificant.
3. The liquid viscosity is assumed to be uniform and that of water at 60°C (the measured wall temperature). The residence time scale, computed as the liquid residence length in the heated region before it reaches the bubble divided by the bulk flow velocity, is approximately 2.5 s. This time scale is much greater than the heat diffusion time scale (approximately

0.067 s), the time required for liquid to reach uniform temperature via heat diffusion from the channel walls. The liquid temperature in the simulated region can thus be assumed to be that of the channel wall (60°C), resulting also in relatively uniform liquid properties such as viscosity.

3.2 Trial geometry construction

Following our first assumption above, we present a schematic of the bubble geometry in Fig. 3b. This construct is used to determine the three-dimensional bubble geometries for a given bubble cross-section at plane P. The bubble cross-sectional shape is first determined by an image-processing algorithm where points outlining the shape of the bubble are selected based on local peak intensities at the interface. These points are then best fit to a circle to determine the center (x_0, y_0) and radius a_0 of the circular segment that outlines the bubble cross-section (see also Fig. 2). The z coordinate of the image center z_p in Fig. 3b is known from the image-to-glass-slide distance d_2. The location of the bubble center (x_0, y_0, z_0) and the (three-dimensional) bubble radius R then completely describe the bubble geometry. Note that the distance of the bubble center (x_0, y_0, z_0) to the image center (x_0, y_0, z_p), d_1, can be related to the bubble radius as

$$R = \sqrt{d_1^2 + a_0^2}, \tag{1}$$

where $d_1 = z_p - z_0$. This constraint implies that a single free parameter, d_1 or R, can be chosen to fully describe the bubble geometry. Note also that the bubble may contact two channel walls, when $R > d$ and/or $R > d_y$, where d and d_y are the distances of the bubble center from the glass and silicon channel walls, respectively, as illustrated in Fig. 3b.

3.3 Numerical iteration scheme with FEMLAB

We vary the single free parameter (R or d_1) and compute the corresponding flow field for an initial trial geometry. The best approximating value for the actual bubble radius $R = R_0$ is chosen based on the closest match between the computed and experimental velocity fields. Our numerical procedure is summarized in Fig. 4. A trial bubble radius of $R \geq a_0$ is chosen and the geometry of Fig. 3b is used to determine d_1 and d. A trial pressure difference is then imposed on the flow.

We use FEMLAB to solve the incompressible three-dimensional Navier–Stokes equations using the finite element method for the liquid-phase only. The flow field is considered steady as per Assumption 2 above. The geometry is created and meshed with the boundaries of the computational domain located at least two diameters upstream and downstream of the nearest bubble surface. (A larger computational domain was used to verify that the pressure gradient at the upstream and downstream boundaries approximately relaxes to the constant value far from the bubble.) The prescribed boundary conditions are as follows: (1) Flow was introduced by an applied pressure difference between the inlet and the outlet; (2) No-slip boundary conditions were prescribed at the channel walls; (3) No-slip boundary conditions were prescribed at the liquid-vapor interface. (The seemingly unconventional choice of a no-slip boundary condition for the bubble interface is discussed in Sect. 4.)

The correct pressure difference across the computational domain was also determined using an interative procedure within each iteration of trial bubble geometry. Upon solving the flow field using a trial pressure difference, the velocities at the inlet are integrated to determine the flow rate. When the inlet flow rate con-

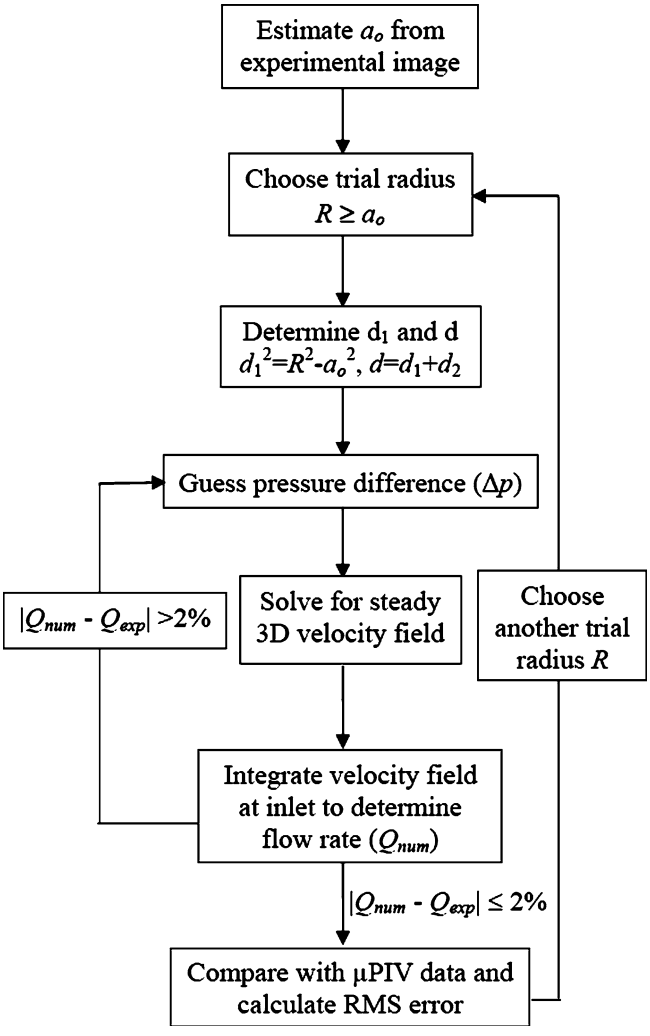

Fig. 4 Iteration scheme used for numerical simulation. The commercial finite element software FEMLAB was used to solve the three-dimensional, steady-state Navier–Stokes equations in the microchannel with trial values of R for each a_0. The applied pressure difference was varied until flow rate matched that of the experiments. For each R, the computed flow field was compared with μPIV data and an RMS error was obtained using Eq. 2. The best approximating radius $R = R_0$ was identified from the minima of the $e_{RMS}(R)$ curves (Fig. 6)

verges to within ±2% of the experimentally measured flow rate, the pressure iteration is completed. The projected two-dimensional flow field at plane P is then compared with the experimental velocity data using a root mean square (RMS) error analysis, defined as

$$e_{\mathrm{RMS}} = \sqrt{\frac{\sum_{i}^{n} (u_{\mathrm{exp},i} - u_{\mathrm{num},i})^2 + (v_{\mathrm{exp},i} - v_{\mathrm{num},i})^2}{\sum_{i}^{n} (u_{\mathrm{exp},i}^2 + v_{\mathrm{exp},i}^2)}}, \quad (2)$$

where u and v denote the velocities in the x and y directions, respectively. The subscript exp denotes the experimental μPIV results, num the numerical results, and the subscript i is the index of points where PIV velocity data is obtained. The sum is over all of the n sampled points.

For each image depth d_2 and instantaneous image radius a_0, we solve for the three-dimensional velocity field, and the function $e_{\mathrm{RMS}}(R)$ is obtained for a range of trial bubble radii R. The best approximating geometry where $R = R_0$ is identified by locating the minimum of the $e_{\mathrm{RMS}}(R)$ curve (Fig. 6), i.e., R_0 satisfies

$$e_{\mathrm{RMS}}(R_0) = \min_{R}[e_{\mathrm{RMS}}(R)]. \quad (3)$$

In Sect. 4, we present and analyze our results based on various available data sets.

4 Results

Figure 5 shows an overlay of best-matched experimental and simulated velocity fields for the case shown in

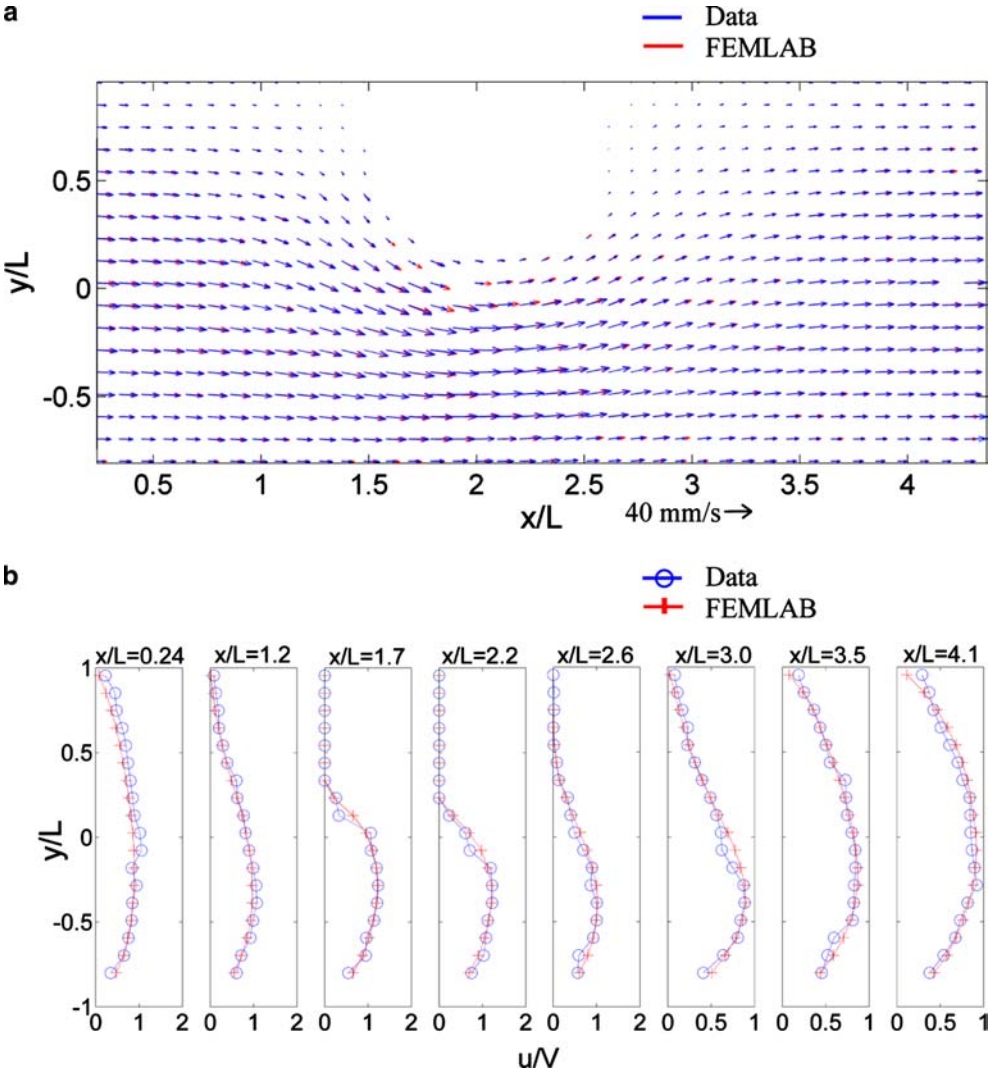

Fig. 5 Exemplary best matched experimental and simulated velocity fields at the focal plane. For this case, the bubble image has a radius of $a_0 = 48.5$ μm at $d_2 = 17.5$ μm from the glass channel wall (Fig. 2). The best approximating bubble radius $R_0 = 53$ μm is captured from the minima of the $a_0 = 48.5$ μm curve in Fig. 6b. Shown in the figure are **a** overlay of experimental and simulated velocity field, and **b** u-velocity slices as a function of y at varying x locations. The length and velocity scales are $L = 100$ μm and $V = 40$ mm/s, respectively. For this case, the calculated RMS error is 12%

Fig. 2, where $a_0 = 48.5$ μm at a focal plane location of $d_2 = 17.5$ μm. $R_0 = 53$ μm is chosen from the minimum of the $a_0 = 48.5$ μm curve in Fig. 6b. The coordinates are nondimensionalized by the half-channel width $L = 100$ μm, and the velocity is nondimensionalized by a characteristic velocity scale $V = 40$ mm/s. The u-velocity profiles at various nondimensionalized x locations in the channel are shown in Fig. 5b. Fairly good agreement is attained between the computed and experimental velocity data, and the RMS error (i.e., discrepancy between measurement and computation) for this particular case is approximately 12%.

Figure 6 shows the RMS error as a function of the trial radius R. Plots 6a, b correspond to various measurement depths (and therefore individual bubble nucleation-to-departure cycles or realizations) of $d_2 = 10$ μm (left) and $d_2 = 17.5$ μm (right), respectively. Each plot contains four curves corresponding to various a_0 values (i.e., different instances during the growth of the bubble). The minimum RMS error of each curve in general ranges from 10 to 20%, and deteriorates as a_0 increases. However, the clear presence of a minimum for each RMS error curve evidently suggests that there is a best approximating bubble geometry and three-dimensional velocity field for each growing bubble at each instant in time. Note the RMS curves cannot be extended further toward the left as the bubble radius R must be equal to or larger than the image radius a_0.

We have also evaluated the efficacy of different boundary conditions in the numerical simulations at the liquid–vapor interface, and the results are shown in Fig. 7. Both slip and no-slip boundary conditions were prescribed for the bubble interface for depths of $d_2 = 10$ μm (left) and $d_2 = 17.5$ μm (right) and for various values of a_0. The RMS errors presented are the minimized error $\min_R[e_{\mathrm{RMS}}(R)]$ (*or* $e_{\mathrm{RMS}}(R = R_0)$) as determined from the R curves in Fig. 6. The results suggest that the no-slip boundary condition consistently results in smaller values of e_{RMS}. This result at first seems to be inconsistent with bubble/liquid interaction, as liquid–gas interfaces are typically modeled using slip boundary conditions (Batchelor 1967). We attribute this result to the presence of surfactants in our experiments (see Sect. 2). While the surfactants decrease the surface tension of the bulk liquid, the important parameter is the hydrodynamic conditions of the interface. Surfactants are known to effectively immobilize bubble surfaces and result in a liquid–vapor interface that acts more like a solid surface (Clift et al. 1978; Levich 1962). Other possibilities such as surface tension spatial variations or

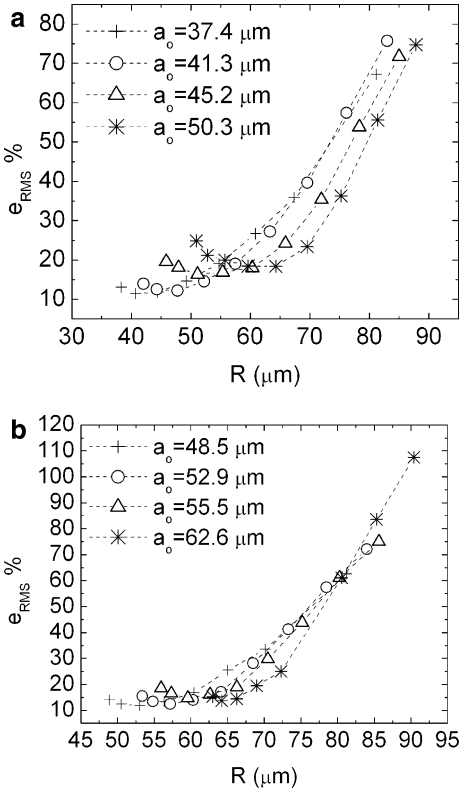

Fig. 6 RMS error (Eq. 2) as a function of the trial bubble radius R for image depths of **a** $d_2 = 10$ μm and **b** $d_2 = 17.5$ μm. Each value of a_0 corresponds to a unique bubble nucleation-to-departure cycle. The best approximating radius $R = R_0$ was extracted from the minima of the curves for each value of a_0

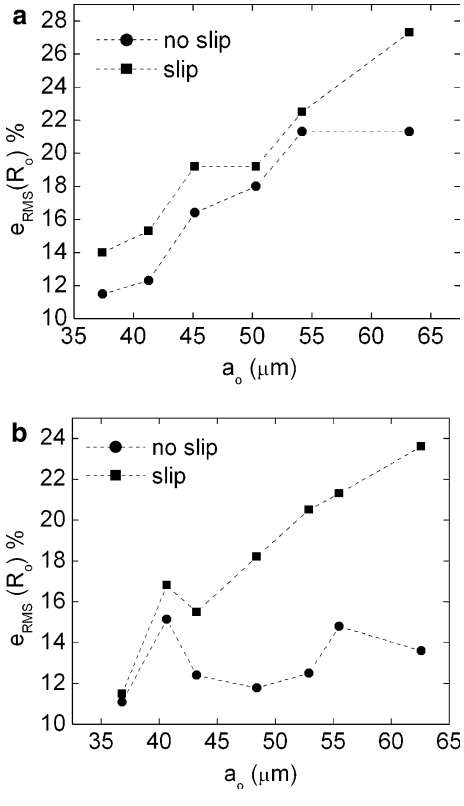

Fig. 7 Minimal RMS errors computed with slip and no-slip boundary conditions prescribed at the liquid–vapor interface, for the cases of **a** $d_2 = 10$ μm and **b** $d_2 = 17.5$ μm. Here, RMS errors are the minimal errors $e_{\mathrm{RMS}}(R_0) = \min_R[e_{\mathrm{RMS}}(R)]$ for each value of a_0 (see Fig. 6). The results suggest the no-slip boundary condition provides a better agreement between the experimental data and numerical simulations

surfactant accumulation at the rear region of the bubble (Levich 1962) may also complicate the boundary conditions. The issue of liquid–vapor hydrodynamic boundary conditions in boiling (and outgassing bubble) flows is a critical area where more work is needed.

Figure 8 examines the movement of the bubble in the depth direction, z, from the glass channel wall as a function of the best approximated bubble radius R_0, for three nucleation realizations measured at $d_2 = 10$, 17.5, and 30 μm. The total distance of the bubble center from the glass channel wall d is obtained where $d = d_1 + d_2$ (Fig. 3b). The results indicate that for $R_0 \leq 55$ μm, there is an approximately linear relation between the distance of the bubble center from the glass channel wall and the bubble radius; whereas for $R_0 \geq 55$ μm no obvious repeatable trend is observed. Most importantly, the agreement of trajectories in the range of $R_0 \leq 55$ μm across values of d_2 (focal depth) suggest a trend in the value of contact angles as discussed below.

The linear dependence of R_0 versus d for $R_0 \leq 55$ μm suggests consistent values of contact angles. As shown in Fig. 3b, the bubble may contact both the channel walls, when $R_0 > d$ and/or $R_0 > d_y$, respectively. The contact angles are given by

$$\theta_g = \cos^{-1}\left(\frac{d}{R_0}\right), \quad \theta_s = \cos^{-1}\left(\frac{d_y}{R_0}\right), \tag{4}$$

where θ_g and θ_s denote the contact angles on the glass and silicon channel walls, respectively. (Note that a contact angle computed according to $\theta_s = \cos^{-1}(d_y/a_0)$, which may be obtained from Fig. 2 alone without the full geometry reconstruction, does not correctly represent the contact angle of the windward and leeward sides of the three-dimensional bubble.) A linear fit (intersecting $d = R_0 = 0$) of the initial d–R_0 curve for $R_0 \leq 55$ μm is presented in Fig. 9a; a fitted value of $d/R_0 = 0.90$ gives a value of $\theta_g = 26°$, which is in close agreement with reported contact angles values (Cubaud and Ho 2004). Similarly, we also plot and fit the d_y–R_0 curves in Fig. 9b and obtain $d_y/R_0 = 0.73$ and $\theta_s = 43°$. This value is within the range of contact angle values for water on silicon. More precise comparisons with past work are difficult as the channel walls used here were etched using the DRIE process which may significantly alter surface roughness.

The agreement of the d–R_0 and d_y–R_0 relations for $R_0 \leq 55$ μm (see Figs. 8, 9) provides evidence that the methodology is consistent. For three measurement planes ($d_2 = 10$, 17.5, and 30 μm), and therefore three independent realizations of bubble nucleation-to-departure cycles, we observed consistent d–R_0 and d_y–R_0 relations as well as similar contact angle values on both glass and silicon channel walls. Because (R_0, d, d_y) completely specify the three-dimensional bubble geometry as well as

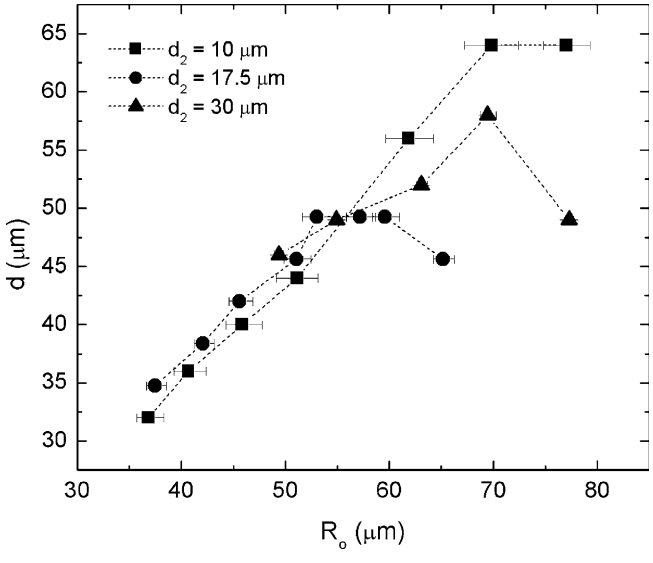

Fig. 8 Bubble center distance in the depth (z) direction, d, as a function of the best approximated radius R_0. The distance d is the distance of the bubble center from the glass channel wall (see Fig. 3). In general, bubble centers move away from the glass channel wall as the bubbles expand. The agreement among data of different depths (various and independent nucleation-to-departure cycles) provides evidence that bubbles repeatedly nucleate at the same site and grow in a repeatable fashion. The initial linear slopes suggest constant contact angle values as shown in Fig. 9

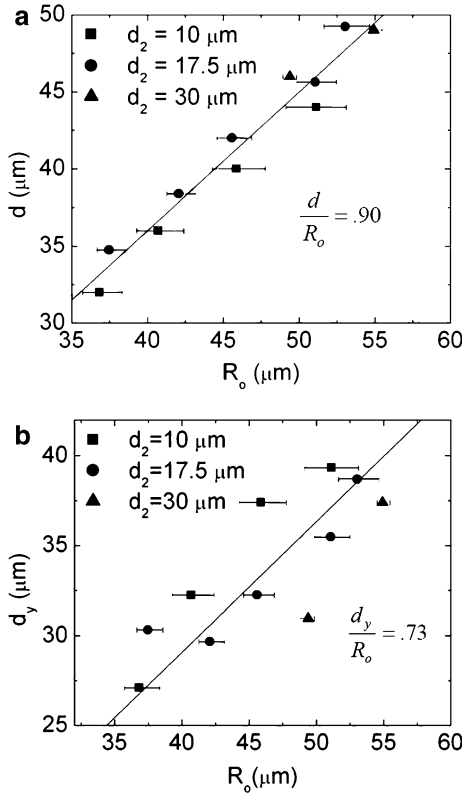

Fig. 9 Parameters determining contact angle for **a** water–glass contact and **b** water–silicon contact. Data for $R_0 \leq 55$ μm from Fig. 8 are extracted and fitted with a straight line (**a**). The computed contact angle (Eq. 4) gives a value of 26° which is in close agreement with reported values in the literature (Cubaud and Ho 2004). Plot **b** shows contact angle extraction for the water–silicon contact in the y direction (see Fig. 3b). Here, the computed value is 43° which is within the range of reported values

location, this agreement among data from different nucleation cycles suggests that the bubbles consistently nucleate at and grow anchored to the same site.

The departure from linearity of the d–R_0 curves for $R_0 \geq 55$ μm in Fig. 8 may be attributed to various causes such as contact angle hysteresis, and/or breakdown of the spherical and steadiness assumptions on which the current methodology is based. Identifying and accounting for the effects of flow-induced deformation of bubble shape and unsteady bubble growth and fluid flow may be needed for the development of more comprehensive bubble departure criteria.

Finally, in Fig. 10 we present the best approximated bubble radius R_0 as a function of time. The growth rates are also approximately linear, and this agrees with the observations reported by Lee et al. (2004). For our flow, this linear growth rate may be particular to the dynamics governing the transport between dissolved gases and the liquid. Further quantitative analysis of growth dynamics needs to be performed to account for effects of outgassing, boiling, and confined geometry flow dynamics, the latter of which is unique to bubble growth patterns in microchannels.

5 Conclusions and future work

We have presented a hybrid methodology that can be used to approximately reconstruct three-dimensional bubble geometry, location, and the associated three-dimensional velocity field during bubble growth and nucleation in a microchannel. We use two-dimensional images, velocity field measurements from μPIV, and numerical simulations from FEMLAB. A measured local bubble nucleation temperature of 60°C suggests most of the nucleation and growth of bubbles we observed was due to outgassing of the liquid. Liquid velocity field measurements were performed at various depths of the channel during bubble growth using μPIV. These image data and two-component velocity data in two-dimensional planes provide only limited information. We performed three-dimensional numerical flow simulations using a range of trial bubble geometries. The best approximating bubble geometry was identified by determining the closest match between computed and experimental velocity fields at the focal plane. The in-plane projection of the predicted three-dimensional velocity field and the μPIV data showed agreement to within 10–20% of our global RMS error scale. Contact angles and bubble growth rates were also estimated from these data. We found that a no-slip boundary condition at the liquid–vapor interface provides a better match between flow predictions and measurements than a slip condition.

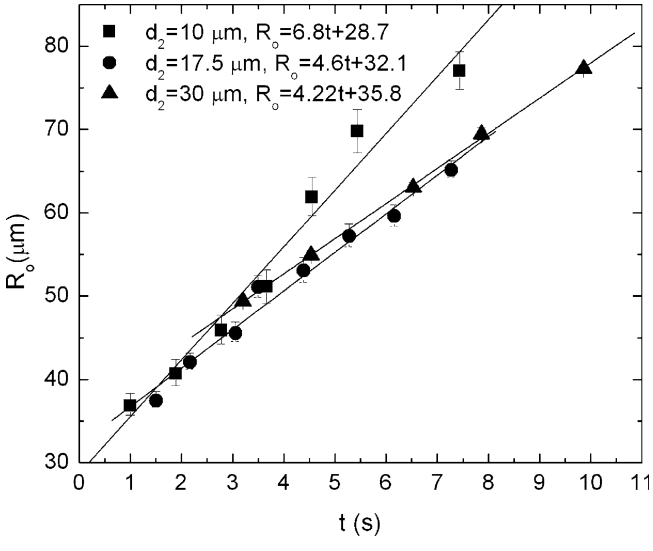

Fig. 10 Best approximated bubble radius R_0 as a function of time and for three positions of the measurement volume. Each data set is shown with a linear regression fit that is provided in the legend

The results obtained from the current work suggest interesting behavior of nucleating vapor bubbles in microchannels. The distance of the bubble center from the glass channel wall increased (roughly linearly) with increasing bubble radii up to approximately $R_0 = 55$ μm, such that constant contact angles were maintained. The contact angles for the glass and silicon channel walls were estimated to be $\theta_g = 26°$ and $\theta_s = 43°$, respectively. The trajectory of the bubble center became less predictable when the bubble grew beyond $R_0 = 55$ μm; this may be attributed to contact angle hysteresis or breakdown of the assumptions used in this analysis. Bubble radius also varied linearly in time. The agreement of our bubble center trajectories and bubble growth rate across different measurement depths also suggests our methodology is consistent.

The current work provides useful insight to modeling bubble dynamics in two-phase microchannel convection. The information obtained contributes toward the understanding of dynamics and mechanisms for bubble growth and departure. Our future work will aim to further obtain quantities such as viscous, pressure, as well as surface forces, with an ultimate goal of establishing a quantitative departure criterion for nucleating bubbles in microchannels.

Acknowledgements This work is supported by the National Defense Science and Engineering Graduate Fellowship (Evelyn N. Wang) and the Microelectronics Advanced Research Corporation (MARCO). The project made use of the National Nanofabrication Users Network facilities funded by the National Science Foundation under award number ECS-9731294.

6 Appendix: uncertainties of the method

In this section, we discuss the estimated uncertainties associated with our hybrid method. In particular, we discuss measurement uncertainty due to perspective projection, Brownian motion, and correlation peak

center determination; all of which influence velocity measurements. We also briefly discuss uncertainties in the methodology due to image depths (d_2) as well as bubble image radius (a_0) determination.

Perspective projection error may contribute to the uncertainty in measurements due to our use of a low numerical aperture objective (NA = 0.45). This objective corresponds to a relatively large measurement depth of 13.5 μm. Perspective error results in a z-velocity component that cannot be decoupled from the in-plane (x, y) velocity measurement in the experimental results. Using the analysis described by Raffel et al. (1998), a large third-dimensional velocity can lead to an upper bound velocity bias of 6 mm/s which is equivalent to an error of approximately 13% for a particle furthest from the center of the objective. This error, however, was minimized by positioning the channel such that the largest out-of-plane velocities are closest to the center of the CCD array. Typical velocity uncertainties due to this effect are approximately 6% in the region near the bubble.

Two additional quantifiable sources of uncertainty in determining the velocity field are Brownian motion and identification of the center of the cross-correlation peak. The uncertainty associated with Brownian motion was ±1% (Devasenathipathy et al. 2003). Uncertainty associated with the identification of the location of the cross-correlation peak was mitigated by ensuring that the peak was distributed over 3–4 pixels, so the center of the cross-correlation peak could be determined to within approximately one-tenth of the particle image diameter (Prasad et al. 1992). The particle image diameter in the focal plane was 1.8 μm, which corresponded to a normalized measurement uncertainty of 180 nm or ±2.2%.

Determination of the focal depth and bubble radius gives rise to uncertainties in bubble location and shape, and contributes to the RMS error difference defined in Sect. 3. Uncertainties associated with determining the location of the focal plane are minimized by examining results from iterations performed at neighboring d_2 values from the measured focal plane. Selection of a focal plane 2.5 μm from d_2 can lead to an RMS error difference of 5–10%. RMS error is also affected by uncertainties in the image radius a_0. The location of the liquid–vapor interface was not always clearly defined as particles that accumulate at the interface are typically out of focus due to light scatter effects such as refraction (see Fig. 2a). The image processing algorithm selected points at the interface based on the peak intensity and located the boundary within variations of 5 μm in radius. We estimate that this yields velocity RMS error differences of 5%.

We can estimate the total contribution to the global RMS error scale by assuming each of these sources of uncertainty are uncorrelated (and taking the square root of the sum of the mean square value of uncertainties). This analysis results in a typical value of about 10% for the value of e_{RMS} as defined in Sect. 3.

References

Batchelor GK (1967) An introduction to fluid dynamics. Cambridge University Press, Cambridge, UK

Clift R, Grace JR, Weber ME (1978) Bubbles, drops and particles. Academic, New York

Cubaud T, Ho CM (2004) Transport of bubbles in square microchannels. Phys Fluids 16(12):4575–4585

Devasenathipathy S, Santiago JG, Wereley ST, Meinhart CD, Takehara K (2003) Particle imaging techniques for microfabricated fluidic systems. Exp Fluids 34:504–514

Hetsroni G, Mosyak A, Segal Z (2001) Nonuniform temperature distribution in electronic devices cooled by flow in parallel microchannels. IEEE Trans Components Packag Technol 24(1):16–23

Hetsroni G, Mosyak A, Segal Z, Ziskind G (2002) A uniform temperature heat sink for cooling of electronic devices. Int J Heat Mass Transf 45:3275–3286

Jiang L, Wong M, Zohar Y (2001) Forced convection boiling in a microchannel heat sink. J Microelectromech Syst 10(1):80–87

Jones SF, Evans GM, Galvin KP (1999) Bubble nucleation from gas cavities: a review. Adv Colloid Interf Sci 80:27–50

Kandlikar SG (2004) Heat transfer mechanisms during flow boiling in microchannels. J Heat Transf 126(1):8–16

Kandlikar SG, Stumm BJ (1995) A control volume approach for investigating forces on a departing bubble under subcooled flow boiling. J Heat Transf 117:990–997

Kennedy JE, Roach GM, Dowling MF, Abdel-Khalik SI, Ghiaasiaan SM, Jeter SM, Quershi ZH (2000) The onset of flow instability in uniformly heated horizontal microchannels. J Heat Transf 122(1):118

Klein D, Hetsroni G, Mosyak A (2005) Heat transfer characteristics of water and APG surfactant in solution in a micro-channel heat sink. Int J Multiphase Flow 31:393–415

Lee PC, Tseng FG, Pan C (2004) Bubble dynamics in microchannels. Part I: single microchannel. Int J Heat Mass Transf 47:5575–5589

Levich VG (1962) Physicochemical hydrodynamics. Prentice-Hall, Englewood Cliffs, NJ

Levy S (1967) Forced convection subcooled boiling-prediction of vapor volumetric fraction. Int J Heat Mass Transf 10:951–965

Li J, Cheng P (2004) Bubble cavitation in a microchannel. Int J Heat Mass Transf 47:2689–2698

Lindken R, Merzkirch W (2000) Velocity measurements of liquid and gaseous phase for a system of bubbles rising in water. Exp Fluids 29:S194–S201

Lindken R, Merzkirch W (2002) A novel PIV technique for measurements in multiphase flows and its application to two-phase bubble flows. Exp Fluids 33:814–825

Liu D, Garimella SV, Wereley ST (2004) Infrared micro-particle image velocimetry of fluid flow in silicon-based microdevices. Heat transfer/fluids engineering summer conference. Charlotte, NC

Meinhart C, Wereley ST, Gray MHB (2000) Volume illumination for two-dimensional particle image velocimetry. Measure Sci Technol 11:809–814

Meinhart CD, Wereley ST, Santiago JG (2005) A PIV algorithm for estimating time-averaged velocity fields. J Fluids Eng 122(2):285–289

Mukherjee A, Kandlikar SG (2005) Numerical simulation of growth of a vapor bubble during flow boiling of water in a microchannel. Microfluidics and Nanofluidics 1(2):137

Murphy RC, Bergles AE (1972) Subcooled flow boiling of fluorocarbons-hysteresis and dissolved gas effects on heat transfer. In: Proceedings of Heat Transfer and Fluid Mechanics Institute, Stanford University Press, Stanford, pp 400–416

Park JS, Kihm KD, Allen JS (2002) Three-dimensional microfluidic measurements using optical sectioning by confocal microscopy. ASME international mechanical engineering congress and exposition. New Orleans, Louisiana

Park JS, Choi KC, Kihm KD (2004) Optically sliced micro-PIV using confocal laser scanning microscopy. Exp Fluids 37:105–119

Peng XF, Wang B-X (1993) Forced convection and flow boiling heat transfer for liquid flowing through microchannels. Int J Heat Mass Transf 36(14):3421–3427

Prasad AK, Adrian RJ, Landreth CC, Offutt PW (1992) Effect of resolution on the speed and accuracy of particle image velocimetry interrogation. Exp Fluids 13:105–116

Qiu D, Dhir VK (2002) Experimental study of flow pattern and heat transfer associated with a bubble sliding on downward facing included surfaces. Exp Therm Fluid Sci 26:605–616

Qu W, Mudawar I (2002) Prediction and measurement in incipient boiling heat flux in micro-channel heat sinks. Int J Heat Mass Transf 45:3933–3945

Raffel M, Willert C, Kompenhas J (1998) Particle image velocimetry. Springer, Berlin, Heidelberg, New York

Santiago JG, Wereley ST, Beebe DJ, Adrian RJ (1998) Particle image velocimetry system for microfluidics. Exp Fluids 25(4):316–319

Steinke ME, Kandlikar SG (2004) Control and effect of dissolved air in water during flow boiling in microchannels. Int J Heat Mass Transf 47(8/9):1925

Zhang L, Koo J-M, Jiang L, Asheghi M, Goodson KE, Santiago JG, Kenny TW (2002) Measurements and modeling of two-phase flow in microchannels with nearly-constant heat flux boundary conditions. J Microelectromech Syst 11(1):12–19

Zhang L, Wang EN, Goodson KE, Kenny TW (2005) Phase change phenomena in silicon microchannels. Int J Heat Mass Transf 48(8):1572–1582